Emergence of scale-free smectic rivers and critical depinning in emulsions driven through disorder

Marine Le Blay[a,b], Mokhtar Adda-Bedia[a], and Denis Bartolo[a,1]

[a]Laboratoire de Physique, École Normale Supérieure de Lyon, Université Claude Bernard, Université de Lyon, CNRS, F-69342 Lyon, France; and [b]Pôle d'Etudes et Recherche de Lacq, Total SA, BP 47-64170 Lacq, France

Edited by David A. Weitz, Harvard University, Cambridge, MA, and approved May 6, 2020 (received for review January 14, 2020)

During the past 60 min, oil companies have extracted 6 trillion liters of oil from the ground, thereby giving a striking illustration of the impact of multiphase flows on the world economy. From a fundamental perspective, we largely understand the dynamics of interfaces separating immiscible fluids driven through heterogeneous environments. In stark contrast, the basic mechanisms ruling the transport of fragmented fluids, such as foams and emulsions, remain elusive with studies mostly limited to isolated droplets and bubbles. Here, we demonstrate that the mobilization of emulsion driven through model disordered media is a critical plastic depinning transition. To elucidate this collective dynamics, we track the trajectories of hundreds of thousands of microfluidic droplets advected through random lattices of pinning sites. Their dynamics reveals that macroscopic mobilization only requires the coordinated motion of small groups of particles and does not involve any large-scale avalanches. Criticality arises from the interplay between contact and hydrodynamic interaction, which channel seemingly erratic depinning events along smectic river networks correlated over system spanning scales. Beyond the specifics of emulsion transport, we close our article discussing the similarities and profound differences with the plastic depinning transitions of driven flux lines in high-T_c superconductors, charged colloids, and grain transport in eroded sand beds.

transport | heterogeneous media | dynamical phase transition | plastic depinning

From enhanced oil recovery to water remediation, a number of industrial processes having a prominent impact on the world economy and environment rely on multiphase flows in heterogeneous media. Since the early days of oil production, engineers noticed that the displacements of confined immiscible fluids result in inhomogeneous spatial patterns limiting oil extraction from rocks and soils (1). Since then, these patterns have been extensively studied by fluid mechanics, statistical physicists, and engineers (2–5).

However, our understanding has remained strongly unbalanced. The imbibition and drainage patterns formed by moving interfaces separating immiscible fluids have been extensively investigated (2–9). Conversely, the collective dynamics of fragmented interfaces in foams and emulsions remains virtually uncharted territory, although relevant to a number of practical situations (10–13). Understanding the displacement of say oil-in-water emulsions in a natural porous medium is a formidable challenge that remains out of reach of current physical investigations. In principle, it requires addressing at once the transport, the coalescence, the fragmentation, and the coarsening of the droplets, modeling multiscale flows and their interplay with the droplets' shape and speed (14, 15). Until now, aside from rare exceptions, most physics studies have therefore focused on the microscopic mechanisms occurring at the pore scale, or on flows past isolated obstacles (16–21).

From a broader perspective, the transport of interacting particles driven through disordered media is an essential aspect of nonequilibrium physics in systems as diverse as driven flux lines and skyrmion textures in condensed matter, colloidal transport, and sand-bed erosion (5, 22–24). Unlike driven elastic systems (4, 5, 25, 26), such as contact lines, Abrikosov lattices, or magnetic domain walls, the situation where collections of driven particles undergo plastic flows through disordered media lacks quantitative model experiments to build a unified framework (22–24, 27, 28). We intend to rectify this situation.

In this article, we introduce a model experiment to address the plastic depinning of particles hydrodynamically driven through heterogeneous environments. In the spirit of the seminal work by Saffman and Taylor (29), we consider a minimal geometry and flow monodisperse emulsions past random lattices of pinning sites in two-dimensional (2D) microchannels. We find a sharp dynamical transition between a creeping regime where the droplets undergo finite displacements and a flowing regime where a finite fraction of the emulsion is effectively mobilized through sparse static rivers. We establish the critical nature of this mobilization transition and demonstrate the smectic symmetry of the resulting flow patterns. We show that criticality does not arise from scale-free avalanches, or large-scale dynamical heterogeneities, but stems instead from hydrodynamic focusing through self-organized river networks correlated over system spanning scales. We conclude our article discussing the essential similarities and difference between hydrodynamic mobilization, plastic depinning in dirty superconductors (22), granular erosion (24, 30), and Darcy flows in yield stress fluids (31, 32).

Significance

Processes as diverse as enhance oil recovery, sand-bed erosion, and even transport of magnetic flux lines in dirty superconductors ultimately rely on the displacement of interacting particles (oil droplets, grains, or flux lines) through disordered media. In all these examples, a minimal drive is required to unpin and transport interacting particles. Taking advantage of model microfluidic experiments, we demonstrate that the depinning of emulsions advected through disordered channels is a critical phenomenon: a phase transition between a regime where the droplets are trapped and a flowing regime where the droplets are effectively transported through an emergent network of sparse rivers. These experiments illuminate the universality of plastic depinning dynamics.

Author contributions: D.B. designed research; M.L.B. performed research; M.L.B., M.A.-B., and D.B. analyzed data; and M.L.B. and D.B. wrote the paper.

The authors declare no competing interest.

This article is a PNAS Direct Submission.

Published under the PNAS license.

Data deposition: Data are available at Figshare (https://figshare.com/articles/Figure_data/12240206).

[1]To whom correspondence may be addressed. Email: denis.bartolo@ens-lyon.fr.

This article contains supporting information online at https://www.pnas.org/lookup/suppl/doi:10.1073/pnas.2000681117/-/DCSupplemental.

First published June 8, 2020.

Downloaded at Palestinian Territory, occupied on December 22, 2021

www.manaraa.com

Experiments in Patterned Microfluidics

Our experimental setup is sketched in Fig. 1*A* (*Materials and Methods*). We form a monodisperse emulsion of hexadecane at a T junction in an aqueous solution of glycerol (40 wt %), surfactant (sodium dodecyl sulfate [SDS] 0.1 wt %), and fluorescent dye. The SDS surfactant prevents coalescence and wetting of the channel walls by the hexadecane droplets (Fig. 1*B*). The resulting stable emulsion is injected in a 4.5-cm long and 2-cm wide Hele–Shaw cell through a homogenizer module. In the main channel of height 60 μm, the drops are squeezed and have a pancake shape of radius $a = 47\ \mu$m (Fig. 1 *B* and *C*). Each experiment is initialized injecting three pore volumes of the emulsion at a solvent flow rate $Q = 15\ \mu$L/min (Movie S1). When the injection stops, we are left with a uniform distribution of droplets with an area fraction of 0.70 ± 0.01 if not specified otherwise.

We introduce disorder by patterning the bottom wall of the main channel with circular wells of radius 20 μm and depth 20 μm (Fig. 1 *A* and *B*). As extensively studied in ref. 33, when a droplet contacts a well, it deforms, relaxes its surface energy, and therefore gets pinned by the well (Fig. 1 *B* and *C*). In our experiments, the pinning-well centers are uncorrelated in space; they are distributed according to Poisson distributions (Fig. 1*A*). We use three random lattices, which we characterize by the average number of pinning-site centers per droplet: $\rho_p = 1.0$ (two independent realizations) and $\rho_p = 0.54$. As the wells can overlap (Fig. 1*B*), we quantify the disorder strength by measuring the critical depinning flow speed associated with each pinning site. To do so we inject a dilute fraction of droplets in the disordered channel and continuously increase the flow rate. The distribution plotted in Fig. 1*D* defines a typical depinning flow rate $Q_D = 120\ \mu$L/min for isolated droplets. Q_D corresponds to a capillary number $Ca \sim 2 \times 10^{-3}$.

Results

Droplet Mobilization as a Dynamical Phase Transition. We now describe the mobilization of concentrated emulsions. The experiment consists of driving at constant flow rate a collection of droplets trapped by the lattice of pinning site (Movies S2 and S3). We stress that no additional droplet is produced in the course of the mobilization experiment. Tracking the individual trajectories of hundreds of thousands oil droplets, we distinguish two qualitatively different regimes illustrated in Fig. 2*A* and Movies S3 and S4.

Creeping regime. At low flow rates, the droplets undergo finite displacements but ultimately remain trapped in the disordered channel. In Fig. 2*A* showing the state of the system after the injection of three pore volumes, we merely observe the formation of locally depleted regions. Comparing the final and initial density fields, we find that only a small fraction of droplets is displaced, and only over a finite distance, thereby forming droplet-depleted regions (Fig. 2*B*). Increasing the flow rate increases the area of the depleted regions and the number of finite displacements events.

Mobilization regime. Macroscopic patterns emerge above a critical flow rate $Q^\star$ that increases with the pinning-site density (Fig. 2*A*). Virtually all droplets contribute to the formation of a sparse network of branched and reconnected rivers percolating throughout the entire system (Fig. 2 *A* and *B*). Remarkably, when the number densities of droplets and pinning sites are equal, $Q^\star = 3.5\ \mu$L/min is 30 times smaller than the individual depinning threshold $Q_D = 120\ \mu$L/min, thereby revealing the cooperative nature of the mobilization transition that we discuss below.

The mobilization patterns reflect the net transport of the particles. In Fig. 2*C*, we plot the variations of the number of droplets $\mathcal{N}(t)$ as a function of time. In the creeping regime, almost no droplets are extracted. Conversely, in the mobilization regime a finite fraction of the droplets escapes the channel. The transition between the two dynamics is sharp. Inspecting the variation of the fraction of mobilized droplets, Φ_M, as a function of the applied flow (Fig. 2*D*), we find that Φ_M bifurcates from zero to a finite value when Q reaches $Q^\star$. In order to distinguish between a sharp cross-over and a genuine dynamical transition, we first plot the time τ needed to reach a stationary state in Fig. 2*E*. Importantly, we compare the different timescales normalizing τ by a flow rate-dependent timescale $t_0(Q)$. It is defined as the advection time over a distance equals to one droplet radius a, for a free droplet. In the creeping regime, τ/t_0 is vanishingly small as the droplets hardly move over a single diameter. Conversely, deep in the mobilization regime τ converges toward the free advection time over the entire observation window. However, the variations of τ are nonmonotonic and sharply increase in the vicinity of $Q^\star$ where τ/t_0 is three orders of magnitudes larger than in the creeping regime.

This behavior is suggestive of critical slowing down. To confirm the hypothesis of a critical scenario, we measure the variations

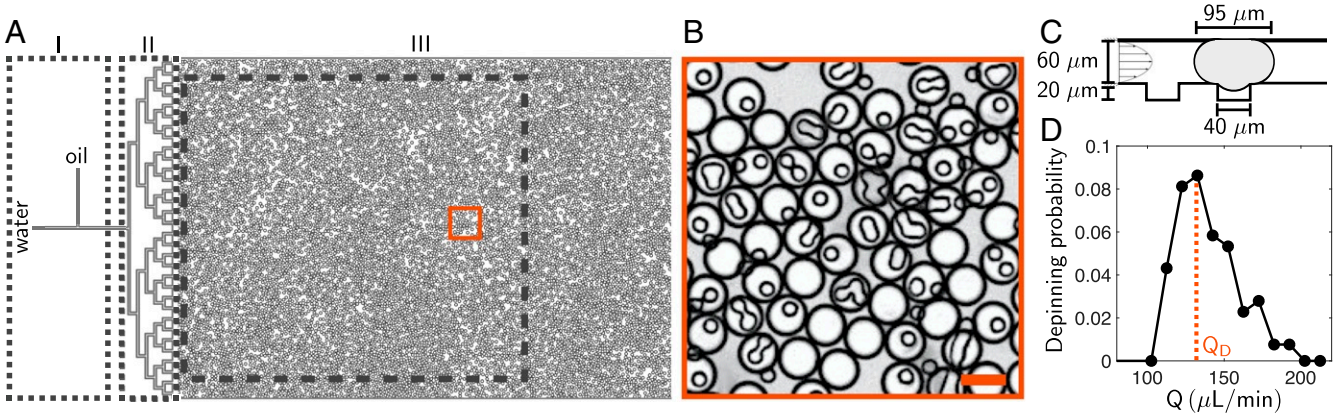

Fig. 1. Microfluidic experiment. (*A*) Sketch of an empty microfluidic device composed of three modules. (*A*, *I*) A T junction is used to produce monodisperse droplets of hexadecane in a water–glycerol solution. (*A*, *II*) A homogenizer module splits the droplet stream into 32 parallel channels. (*A*, *III*) The main microfluidic channel is fed with the monodisperse emulsion. It includes a random lattice of overlapping circular wells of diameter 40 μm. In this picture, the relative density of pinning sites is $\rho_p = 1.0$. We perform our measurement in the window delimited by the dashed line. (*B*) Close-up on an 800 $\times$ 800-μm window showing pinned and free droplets. The small circles are the pinning wells; the large circles are the oil droplets. Note that some of the wells overlap and that no droplet coalesce. (Scale bar: 100 μm.) (*C*) Sketch of a squeezed droplet pinned by cylindrical well. Side view. (*D*) Probability distribution function of the depinning flow rates measured on a dilute ensemble of monodisperse droplets. The distribution is peaked on the typical value $Q_D = 120\ \mu$L/min.

Downloaded at Palestinian Territory, occupied on December 22, 2021

www.manaraa.com

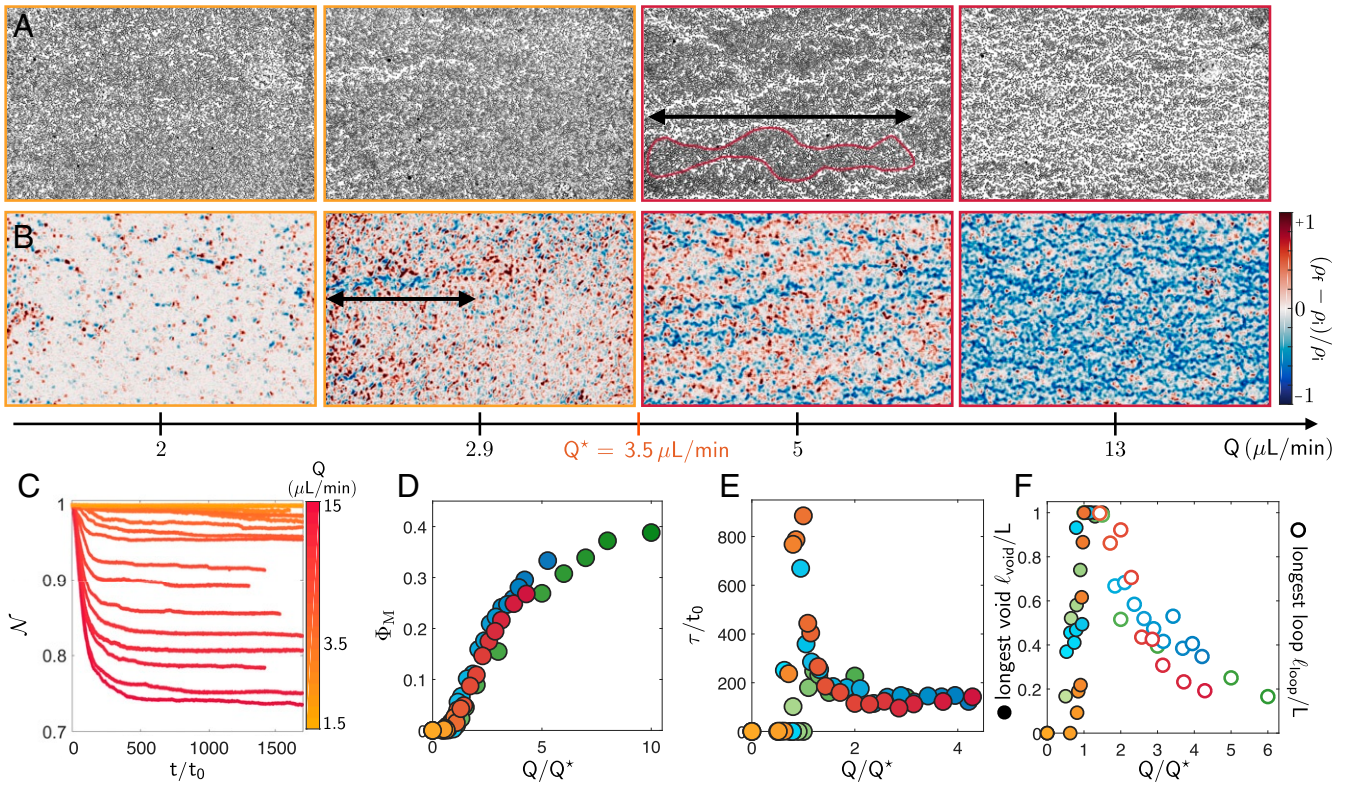

Fig. 2. The mobilization of emulsion through a disordered microfluidic channel is a critical dynamical transition. (*A*) Bright-field images of the droplets (dark dots) in the disordered channel after the injection of three pore volumes at increasing flow rates Q. $\rho_p = 1.0$. (*B*) The color map indicates the difference between the local droplet density at the end and at the beginning of the experiments. Red (blue) regions indicate a local increase (decrease) of the density. Same experiments as in *A*. (*C*) Variations of the overall droplet fraction $\mathcal{N}$ as a function of time in the same device. Time is normalized by t_0, the typical time it takes for a free droplet to move over its own radius. (*D*) Fraction of droplets mobilized out of the system plotted as a function of the normalized flow rate for three different disorder densities (orange symbols: $\rho_p = 1.0$; blue symbols: $\rho_p = 1.0$ [independent disorder realization]; green symbols: $\rho_p = 0.54$). All plots collapse on a single master curve. $Q^\star = 3.5,\ 1.0 \pm 0.1$ μL/min when $\rho_p = 1.0,\ 0.54$, respectively. (*E*) Same color code as in *D*. The normalized relaxation time of $\mathcal{N}(t)$ defined as $\tau/t_0 = (1/t_0)\int_0^\infty [\mathcal{N}(t) - \mathcal{N}(\infty)]dt$ peaks at $Q = Q^\star$. (*F*) Same color code as in *D* and *E*. Filled symbols: length of the longest depleted void measured when $Q < Q^\star$ (*B*). Open symbols: length of the longest loop formed in the river network (*A* and *SI Appendix*). Both length scales grow nonlinearly with Q and peak at the onset of mobilization.

of two typical length scales associated with the mobilization patterns: the length ℓ_{void} of the largest depleted void in the creeping regime and the size of the largest loop ℓ_{loop} of the river patterns in the mobilization regime (Fig. 2 *A* and *B*). We show in Fig. 2*F* that both length scales diverge at the onset of mobilization for all pinning-site densities. Altogether, the sharp bifurcation of Φ_M, the divergence of the relaxation time, and the divergence of the length scales characteristic of the rivers' geometry establish the critical nature of the mobilization transition. This conclusion is further supported by the collapse of all plots in Fig. 2 *D–F* on three master curves independent of the density of disorder: criticality is a robust feature of emulsion mobilization.

Critical Flow Rate. To gain more insight on the mobilization transition, we now investigate the migration dynamics of the droplets. Fig. 3*A* shows an instantaneous map of the longitudinal component of the droplet-velocity field $v_\parallel(\mathbf{r}, t)$, when the droplet extraction rate is maximal (*SI Appendix*). In both regimes, droplet motion takes the form of localized bursts of activity involving clusters of droplets at contact (Movies S2–S5). These localized events seem homogeneously distributed in space, reflecting the nucleation and intermittent growth of depleted regions across the whole sample. Unlike elastic depinning of elastic solids and interfaces, the plastic flows at the onset of mobilization are not supported by large-scale avalanches (5). The absence of avalanches is confirmed by measurements of the number of droplets in each moving cluster. The typical number of droplets in a cluster is comprised between two and eight, hardly depends on ρ_p and does not diverge at $Q^\star$ (Fig. 3*C* and *SI Appendix*). Criticality does not stem from scale-free dynamical heterogeneities.

The finite size of the local flow bursts informs us on the coordinated action of lubricated contacts and geometrical flow focusing at the onset of mobilization. The small value $Q^\star = Q_D/30$, measured when $\rho_p = 1.0$, can indeed be explained as follows. The depinning of an isolated particle is driven by the pressure drop over its own diameter (33). As $\rho_p = 1.0$, one would naively expect Q_D to set the onset of mobilization. However, at $Q^\star$, the pressure drop across a cluster having a typical size of $10a$ along the longitudinal direction is approximately five times larger than across an isolated particle (Fig. 3 *A* and *C*). One would therefore expect $Q^\star$ to be five times smaller that Q_D, which is about an order of magnitude larger than the measured value. This discrepancy is solved noting that droplets at rest form a porous structure that locally focuses the flow of the incompressible continuous phase. A rough estimate of the amplification of the local flow is given by the average porosity of the medium $(1 - \phi)$, where ϕ is the area fraction of the confined emulsion at $t = 0$. Altogether, hydrodynamic focusing and contact interactions give an estimate of $Q^\star$ of the order of ~ 7 μL/min in qualitative agreement with our measurements ($Q^\star = 3.5$ μL/min). We expect this overestimate to originate from the exponential distribution cluster sizes (Fig. 3*C*) and flow heterogeneities reported in similar porous structures (15).

Downloaded at Palestinian Territory, occupied on December 22, 2021
www.manaraa.com

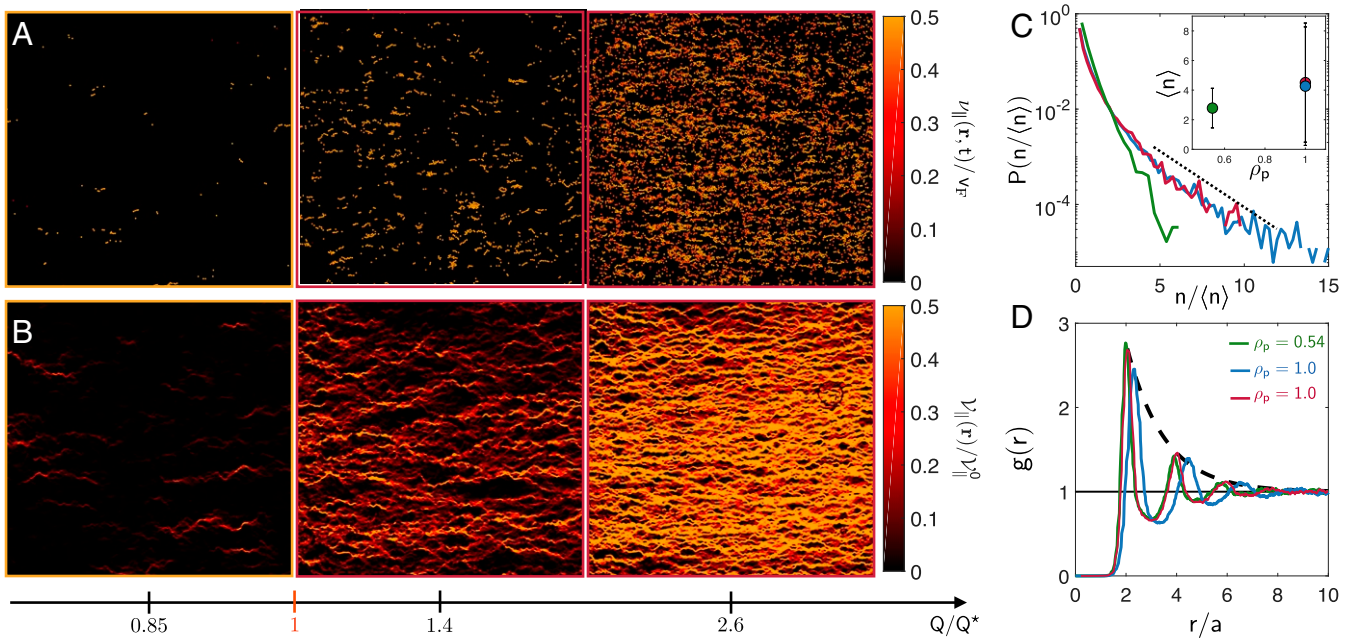

Fig. 3. The droplets are mobilized through a smectic network of channels. (*A*) Instantaneous droplet-velocity field. The color indicates the magnitude of the longitudinal component $\nu_\parallel(\mathbf{r}, t)$ evaluated at the time where the slope of the $\mathcal{N}(t)$ curve is maximum (Fig. 2*C*). (*B*) Map of the maximal droplet flux $\mathcal{V}_\parallel(\mathbf{r})$: a filamentous river network forms above $Q^\star$ (*SI Appendix*). (*C*) Probability distribution function of the number of droplets forming a moving cluster at $Q = Q^\star$. (*Inset*) Mean cluster size. Same color code as in Fig. 2. The number of droplets in a mobilized cluster is exponentially distributed with an average value of the order of five particles. (*D*) Radial distribution function of the droplets at the beginning of the experiment when $Q = 0$ for the three disorder realizations. The dashed line indicates the best exponential fit of the envelope for $\rho_p = 1.0$. $g(r)$ peaks at $r = 2a$ and decorrelates over distance smaller than two diameters for all disorder densities. The difference in the structure of the emulsions for the two experiments performed at $\rho_p = 1.0$ originates from a small difference (15%) in the droplet packing fraction.

Similarly, we can explain why the density of pinning sites does not affect the size of the moving clusters at the onset of mobilization. The emulsions we study have a packing fraction of 0.7. The corresponding pair correlation functions $g(r)$ shown in Fig. 3*D* hardly vary as ρ_p increases. The maximum of $g(r)$ is located at $r = 2a$. The pair correlation function shows very little translationnal order (it decays exponentially over 1.5 drop diameters). These features reflect a structure where the droplets form close-packed clusters of approximately six particles with very little structural correlation. This structure controls the size of the moving clusters. Wherever a local fluctuation in the flow field exists, the resulting excess force on a droplet is mechanically transmitted to all particles in (lubricated) contact. Given the structure of the emulsion, the number of particles in close contact is set by the correlation length of the close-packed cluster. At the onset of mobilization, regardless of the value of ρ_p, we therefore expect the number of particles in a moving cluster to be of the order of approximately six particles. This estimate agrees with all our measurements performed in the three random lattices (Fig. 3*C*). We expect this scenario to be modified only at the onset of contact percolation, in much denser emulsions, where a markedly different depinning dynamics was reported numerically in ref. 34.

A Scale-Free Smectic Network. We now characterize and elucidate the geometry of the river pattern. To do so, we first define the maximal droplet flux $\mathcal{V}_\parallel(\mathbf{r}) = \max_t\left[\nu_\parallel(\mathbf{r}, t)\right]_t$, which continuously bifurcates from zero to a finite value at $Q^\star$, when averaged over space (Fig. 4*A*). Remarkably, the spatial fluctuations of $\mathcal{V}_\parallel(\mathbf{r})$ reveal that the seemingly erratic activity bursts seen in Fig. 3*A* are actually strongly correlated in space. A direct comparison between Figs. 2*A* and 3*B* indicates that nearly all depinning events occur along the sparse river networks seen in the final images of our experiments. From a Lagrangian perspective, this dynamics translates into a bimodal distribution of the individual droplet speed ν_i normalized by the average flow speed v_F in Fig. 4*B*. The localization of the droplet dynamics explains why only 40% of them can be effectively extracted out of the device, even at the highest flow rates.

In order to quantitatively characterize the geometry of the river network, we compute the two point correlations of the $\mathcal{V}_\parallel$ field, $C_\mathcal{V}(x, y)$. The spatial variations of $C_\mathcal{V}(x, y)$ exhibit three essential features. 1) The velocity correlations decay exponentially with marked oscillations along the transverse direction (Fig. 4*C*). These oscillations reflect the periodicity of the river pattern along the y axis with a period $\lambda = 2a$ irrespective of the magnitude of the flow rate and of the pinning-site density ρ_p. Remarkably, the emergence of transverse translational order coincides with the onset of mobilization. We demonstrate this structural transition by plotting the magnitude of the oscillations, $S = C_\mathcal{V}(0, 2a) - C_\mathcal{V}(0, a)$, as a function of the flow rate in Fig. 4*D* and show that S continuously bifurcates from 0 to a finite value at $Q^\star$. 2) The correlations of $\mathcal{V}_\parallel$ decay algebraically along the flow direction: $C_\mathcal{V}(x, 0) \sim x^{-\alpha}$ with $0.5 < \alpha < 1$ (Fig. 4*E*). The smectic river patterns are therefore critical over the entire mobilization regime. 3) The 2D variations of $C_\mathcal{V}(x, y)$ hint toward a microscopic explanation for the rivers' geometry. The oscillatory decay of $C_\mathcal{V}(x, y)$ indeed persists only when the distance vector $\mathbf{r}$ makes an angle larger than $\pi/4$ with respect to the longitudinal axis (Fig. 4*F*). This angle corresponds to the direction where a dipolar flow perturbation changes its sign along the longitudinal axis, thereby suggesting the following picture.

Dipolar Interactions and Flow Focusing. We explain first how contact interactions shape the mobilization patterns into smectic river. We then account for their persistence in time by the channeling of the solvent flow. Let us consider the initial configuration sketched in Fig. 4*G* where the orange droplet undergoes a finite displacement (advection or depinning). If they were

Downloaded at Palestinian Territory, occupied on December 22, 2021

www.manaraa.com

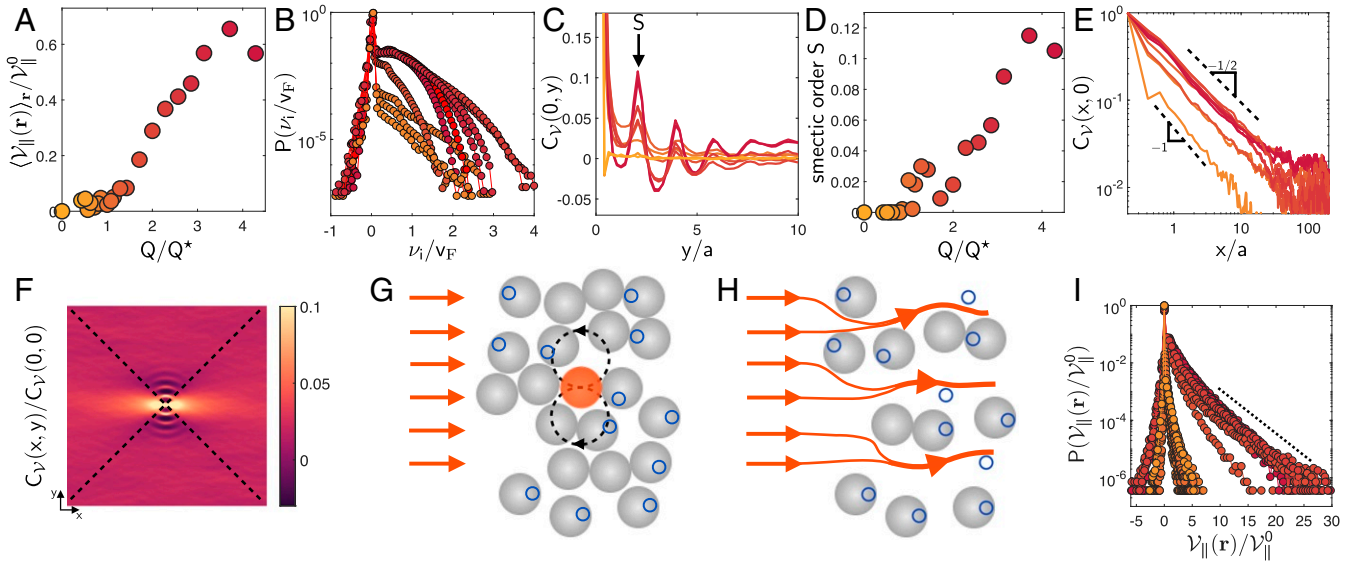

Fig. 4. Smectic rivers, dipolar interactions, and flow focusing. For the sake of clarity, we only present here the data for $\rho_p = 1.0$. The plots corresponding to $\rho_p = 1.0$ (independent realization) and 0.54 are presented in *SI Appendix*, Figs. S2 and S3. (*A*) Spatial average of the maximal droplet flux $\langle \mathcal{V}_\parallel(\mathbf{r})\rangle_\mathbf{r}$ plotted vs. Q. The droplet flux $\langle \mathcal{V}_\parallel(\mathbf{r})\rangle_\mathbf{r}$ bifurcates at $Q^\star$. (*B*) Histogram of the individual droplet speed (along the longitudinal direction). The bimodal distribution reveals the formation of sparse flowing rivers as in ref. 35. (*C*) Decorrelations of the longitudinal flux $\langle \mathcal{V}_\parallel(\mathbf{r})\rangle_\mathbf{r}$ along the direction y transverse to the flow. (*D*) The smectic order parameter $S = C_\mathcal{V}(0, 2a) - C_\mathcal{V}(0, a)$ bifurcates at $Q = Q^\star$. Nematic rivers of width $2a$ emerge at the onset of mobilization. (*E*) Along the longitudinal x direction, the correlations of the droplet flux decay algebraically. $C_\mathcal{V}(x, 0) \sim x^{-\alpha}$ with $0.5 < \alpha < 1$. (*F*) 2D variations of the flux correlations: $C_\mathcal{V}(x, y)$. The dashed lines indicate the directions making angles of $\pi/4$ and $3\pi/4$ with the x axis. The suppression of the oscillations past the dashed lines hints toward the formation of dipolar force chains. (*G*) Sketch of the dipolar displacements induced by the depinning of one droplet in a contact cluster. (*H*) The focusing of the driving flow along the low-density regions promotes and stabilizes mobilization along filamentous rivers. (*I*) Distribution of the instantaneous and droplet flux $\nu_\parallel(\mathbf{r}, t)$ measured at the time where the decay rate of $\mathcal{N}(t)$ is maximal. The local droplet current is distributed according to an exponential distribution. This measurement contrasts with the power law reported in erosion experiments and simulations (24, 30).

all free to move, the surrounding particles would experience a dipolar perturbation to their motion. This behavior (36) merely follows from mass conservation and therefore, applies to the quasistatic displacements, or force distributions, in any ensemble of nearly incompressible particles (see, e.g., ref. 37 for a neat example in a granular medium). Mass conservation implies that the divergence of the particle current vanishes, and at lowest order in gradients, a local particle displacement along the direction $\hat{\mathbf{p}}$ at the origin corresponds to a localized dipolar perturbation: $\nabla \cdot \mathbf{j}(\mathbf{r}) \sim \hat{\mathbf{p}} \cdot \nabla \delta(\mathbf{r})$. The resulting displacements share the same symmetry and are screened over a distance comparable with a particle size (algebraically or exponentially) (38–40). The consequences of this dipolar perturbation are illustrated in Fig. 4*H*. Particles in the downstream region are further pushed, thereby promoting the formation of a directed river. Conversely, the depinning of the particles located above and below the moving one is hindered by the dipolar contact-force network pushing in the direction opposite to the driving flow. Farther away, in the transverse direction, the dipolar perturbation vanishes, and the driving fluid can freely contribute to particle depinning. All together, these contact mechanisms promote, on average, the formation of river lanes along the flow direction. We stress that this mechanism is not specific to depinning physics (13, 22, 41, 42). Similar lanning patterns have been consistently reported experimentally and numerically when ensembles of particles are driven along opposite directions. From charged colloids to self-propelled particles, they all form lively lanning patterns associated with dipolar perturbations inducing transverse structural oscillation and algebraic longitudinal correlations (see, e.g., refs. 40 and 43–45).

Unlike in conventional plastic depinning (22, 42), in our experiments the smectic rivers persist in time. This distinction stems from the specific interplay between the hydrodynamic drive and the spatial structure of the particles. The formation of a river locally increases the permeability of the medium and therefore, facilitates the fluid flow along this anisotropic region of space. This hydrodynamic focusing stabilizes the rivers and hence prevents them from shrinking or widening. In conclusion, the coordinated action of lubricated contact interactions and hydrodynamic focusing explains the self-organization of the droplet flow into a directed river patterns.

Discussion

The mobilization of emulsions in our disordered microfluidic channels realizes a prototypical example of a plastic depinning transition. Plastic depinning was introduced first in the context of flux-line transport in high-T_c superconductors (22, 35, 46–48) and further extended to driven soft matter (22–24, 27–30). Simply put, it defines a flow transition in ensembles of interacting units driven by a constant force through a disordered landscape of pinning sites. Regardless of the microscopic nature of the driven units, plastic depinning is a dynamical phase transition separating an absorbing static state and a flowing state where a finite fraction of the particles is driven through filamentous patterns (22). Although experiments remain scarce, and no unified theory exists, a number of quantitative simulations provide a consistent phenomenology (22, 42): 1) in 2D, the transition is critical (22, 30, 46); 2) plastic flows are associated with a bimodal speed distribution (23, 35); and 3) the instantaneous flows occur along sparse networks of interconnected rivers having a smectic structure deep in the flowing regime (22, 42, 49). Our experiments enjoy these three distinctive properties.

However, two noticeable differences exist between conventional plastic depinning and emulsion mobilization. First, numerical simulations and mean-field models predict an algebraic flux distribution of the plastic flows qualitatively confirmed by granular erosion experiments (24, 30). In contrast, the distribution of the emulsion flux is clearly exponential in Fig. 4*I*. Second,

Downloaded at Palestinian Territory, occupied on December 22, 2021
www.manaraa.com

in "dry" plastic depinning, the river networks continuously rearrange their structure in time, ultimately involving the motion of all particles (24, 35, 42). The patterns shown in Figs. 2*A* and 3*B* and Movie S3 have a markedly different dynamics. After formed, the river network is frozen in time and merely allows a subset of droplets to explore a finite fraction of space: both the creeping and the mobilization regimes are absorbing states for a macroscopic fraction of the driven particles.

We argue that these essential differences stem from the interplay between the hydrodynamic drive and the pattern geometry. Unlike conventional plastic flows, emulsion mobilization is not the response to a constant drive. As a void forms, it locally increases the permeability of the medium, focuses the flow of the driving fluid, and locally amplifies the local force on the arrested droplets, which are more easily mobilized. The formation of the river network is therefore a self-organization process reminiscent of the Laplacian growth of viscous fingers (6). Similarly, the self-focusing of the driving flow results in static viscous fingers with a characteristic dendritic geometry that cannot undergo any structural transformation. This picture is further confirmed by wet granular experiments and simulations that resemble our setup in the limit of zero pinning strength (50–52), where the hydrodynamic drive results in channeling geometries akin to Laplacian patterns.

In conclusion, we have established that the critical mobilization of emulsions defines a "universality class" that relies on two essential ingredients. 1) The drive and the interactions must conspire to allow particles to overcome a local mobilization threshold, and 2) the magnitude of the driving force must be amplified by local mobilization events. Beyond the specifics of our experiments, this conclusion is supported by recent numerical simulations and experiments on the displacement of yield stress fluids in a model porous media (31, 32), a system that combines the two necessary ingredients for critical mobilization and that displays a strikingly similar self-organized plastic depinning phenomenology (31).

Conclusion

The collective mobilization of droplets trapped by random lattices of pinning sites results in large-scale patterns, chiefly governed by the interplay between hydrodynamic flows, contact interactions, and capillary pinning force. We therefore expect these generic mechanisms to shape the emergent flow patterns of a broad class of fragmented liquid interfaces driven through confined heterogeneous environments. Beyond the specifics of emulsions, we have established that the hydrodynamic mobilization of soft particles in disordered geometries realizes a rare experimental demonstration of a critical plastic depinning transition. We now need to address the robustness of this collective dynamics to strongly nonlinear interactions between particles and disorder such as coalescence and fragmentation, a formidable yet necessary challenge to elucidate the general transport rules of soft matter in heterogeneous media.

Materials and Methods

Microfabrication. The microfluidic devices are made using the microfluidic sticker method (53). In brief, the fabrication of the stickers is based on the soft imprint of a photocurable resin (NOA 81 Norland). We first make a mold made of two layers of SU8 photoresist (Microchem). The first layer includes the replica of the random lattice of circular wells; the second is a replica of the straight channels. The mold is replicated to make a PDMS stamp. The stamp is used to imprint a thin layer of thiolene-based resin (NOA 81) cast on a glass coverslip. We cure the resin with 7 s of ultraviolet (UV) exposure (20 mW/cm^2; UV lamp Hamamatsu LC8). The microfluidic chip is finally assembled, sealing the sticker with a quartz slide. Adhesion is ensured by an additional UV exposure and thermal curing for 12 h at 90 °C. In order to prevent the wetting of the channel walls by the emulsion droplets, we treat the device as described in ref. 54. A deep UV exposure for 30 min in a Jelight UVO CLeaner 42 makes the NOA 81 surface permanently hydrophilic. The stickers are connected to three injection tubes using homemade connectors.

Microfluidics and Imaging. We use the stickers to make and transport a hexadecane emulsion dispersed in a solution of water, glycerol (40 wt%), surfactant (SDS; 0.1 wt%), and fluorescein (0.2 wt%). To ensure reproducible initial conditions, we use a systematic fluid-injection protocol. First, the sticker is filled with CO_2 that is more soluble in water than air. We then fill the whole device with water–glycerol solution and dissolve all CO_2 bubbles. Finally, using precision syringe pumps (Nemesis; Cetoni), the water–glycerol solution and hexadecane flow rates are fixed to $Q_w = 12\ \mu L/min$ and $Q_h = 3\ \mu L/min$, respectively, at the T junction. In turn, we produce a monodisperse hexadecane in water–glycerol emulsion with a droplet radius of $a = 47\ \mu m$ and a surface fraction in the main channel of 0.7. After the main channel is filled with the emulsion, we stop the hexadecane flow, impose the minimum flow rate possible for the water–glycerol mixture, and let the system to relax for 10 min. The experiment and recording start after imposing the desired flow rate to the aqueous phase.

We record the fluorescence images of the main channel with a Nikon AZ100 using a 6× magnification and a 4-MPix CCD camera (Basler Aviator). In order to correctly track the droplet trajectories, the frame rate is set as follows: 3.3 fps for flow rates lower than $Q = 6\ \mu L/min$ and 10 fps for flow rates higher than $Q = 6\ \mu L/min$.

Detection and Data Analysis. We detect the center of mass of all droplets in the field of view using the ImageJ minima intensity detection function on contrast-enhanced and Gaussian blurred frames (the SD of the Gaussian kernel is taken equal to $a/2$) (55). The droplets are detected with a pixel accuracy. We reconstruct the drop trajectories and measure their instantaneous velocity using the MATLAB function by Blair and Dufresne based on the Crocker and Grier tracking algorithm (56). We compute all of the Eulerian and Lagrangian quantities defined in the text (density, velocity, current fields, droplet speed, etc.) from the droplet instantaneous positions and velocities as detailed in *SI Appendix*.

Data Availability. Data are available at Figshare, https://figshare.com/articles/Figure_data/12240206.

ACKNOWLEDGMENTS. We thank Alexandre Morin, Stéphane Guillet, and Celeste Odier for invaluable help with the experiments. We acknowledge discussions with Alberto Rosso, Cristina Marchetti, Enric Santanach-Carreras, and Matthieu Wyart. We also thank Ezequiel Ferrero for his insightful feedback on our manuscript.

1. S. E. Buckley, M. Leverett, Mechanism of fluid displacement in sands. *Trans. AIME* **146**, 107–116 (1942).
2. R. Lenormand, Liquids in porous media. *J. Phys. Condens. Matter* **2**, SA79–SA88 (1990).
3. M. Sahimi, Flow phenomena in rocks: From continuum models to fractals, percolation, cellular automata, and simulated annealing. *Rev. Mod. Phys.* **65**, 1393–1534 (1993).
4. M. Alava, M. Dubé, M. Rost, Imbibition in disordered media. *Adv. Phys.* **53**, 83–175 (2004).
5. E. E. Ferrero, L. Foini, T. Giamarchi, A. B. Kolton, A. Rosso, Creep motion of elastic interfaces driven in a disordered landscape. arXiv:2001.11464 (30 January 2020).
6. G. M. Homsy, Viscous fingering in porous media. *Annu. Rev. Fluid Mech.* **19**, 271–311 (1987).
7. B. Sandnes, E. Flekkøy, H. Knudsen, K. Måløy, H. See, Patterns and flow in frictional fluid dynamics. *Nat. Commun.* **2**, 288 (2011).
8. B. Zhao, C. W. MacMinn, R. Juanes, Wettability control on multiphase flow in patterned microfluidics. *Proc. Natl. Acad. Sci. U.S.A.* **113**, 10251–10256 (2016).
9. C. Odier, B. Levaché, E. Santanach-Carreras, D. Bartolo, Forced imbibition in porous media: A fourfold scenario. *Phys. Rev. Lett.* **119**, 208005 (2017).
10. A. Payatakes, Dynamics of oil ganglia during immiscible displacement in water-wet porous media. *Annu. Rev. Fluid Mech.* **14**, 365–393 (1982).
11. M. Diphare, E. Muzenda, "Remediation of oil contaminated soils: A review" in *International Conference on Chemical Integrated Waste Management and Environmental Engineering* (2014), pp. 180–184.
12. A. Perazzo, G. Tomaiuolo, V. Preziosi, S. Guido, Emulsions in porous media: From single droplet behavior to applications for oil recovery. *Adv. Colloid Interface Sci.* **256**, 305–325 (2018).
13. A. Mauray, M. Chabert, H. Bodiguel, Yield stress fluid behavior of foam in porous media. arXiv:1906.04103 (10 June 2019).
14. S. S. Datta, H. Chiang, T. S. Ramakrishnan, D. A. Weitz, Spatial fluctuations of fluid velocities in flow through a three-dimensional porous medium. *Phys. Rev. Lett.* **111**, 064501 (2013).
15. K. Alim, S. Parsa, D. A. Weitz, M. P. Brenner, Local pore size correlations determine flow distributions in porous media. *Phys. Rev. Lett.* **119**, 144501 (2017).
16. N. Bremond, A. R. Thiam, J. Bibette, Decompressing emulsion droplets favors coalescence. *Phys. Rev. Lett.* **100**, 024501 (2008).

Downloaded at Palestinian Territory, occupied on December 22, 2021

www.manaraa.com

17. S. Protiere, M. Bazant, D. Weitz, H. A. Stone, Droplet breakup in flow past an obstacle: A capillary instability due to permeability variations. *Europhys. Lett.* **92**, 54002 (2010).
18. S. S. Datta, J. B. Dupin, D. A. Weitz, Fluid breakup during simultaneous two-phase flow through a three-dimensional porous medium. *Phys. Fluids* **26**, 062004 (2014).
19. B. Géraud, S. A. Jones, I. Cantat, B. Dollet, Y. Méheust, The flow of a foam in a two-dimensional porous medium. *Water Resour. Res.* **52**, 773–790 (2016).
20. B. Géraud, Y. Méheust, I. Cantat, B. Dollet, Lamella division in a foam flowing through a two-dimensional porous medium: A model fragmentation process. *Phys. Rev. Lett.* **118**, 098003 (2017).
21. C. Yeates, S. Youssef, E. Lorenceau, New insights of foam flow dynamics in a high-complexity 2D micromodel. *Colloid. Surface. Physicochem. Eng. Aspect.* **575**, 184–198 (2019).
22. C. Reichhardt, C. O. Reichhardt, Depinning and nonequilibrium dynamic phases of particle assemblies driven over random and ordered substrates: A review. *Rep. Prog. Phys.* **80**, 026501 (2016).
23. A. Pertsinidis, X. S. Ling, Statics and dynamics of 2D colloidal crystals in a random pinning potential. *Phys. Rev. Lett.* **100**, 028303 (2008).
24. P. Aussillous, Z. Zou, É. Guazzelli, L. Yan, M. Wyart, Scale-free channeling patterns near the onset of erosion of sheared granular beds. *Proc. Natl. Acad. Sci. U.S.A.* **113**, 11788–11793 (2016).
25. P. Le Doussal, K. J. Wiese, S. Moulinet, E. Rolley, Height fluctuations of a contact line: A direct measurement of the renormalized disorder correlator. *Europhys. Lett.* **87**, 56001 (2009).
26. J. H. Snoeijer, B. Andreotti, Moving contact lines: Scales, regimes, and dynamical transitions. *Annu. Rev. Fluid Mech.* **45**, 269–292 (2013).
27. R. L. Stoop, P. Tierno, Clogging and jamming of colloidal monolayers driven across disordered landscapes. *Commun. Phys.* **1**, 68 (2018).
28. M. P. N. Juniper, A. V. Straube, D. G. A. L. Aarts, R. P. A. Dullens, Colloidal particles driven across periodic optical-potential-energy landscapes. *Phys. Rev. E* **93**, 012608 (2016).
29. P. G. Saffman, G. I. Taylor, The penetration of a fluid into a porous medium or Hele-Shaw cell containing a more viscous liquid. *Proc. R. Soc. Lond.* **A245**, 312–329 (1958).
30. L. Yan, A. Barizien, M. Wyart, Model for the erosion onset of a granular bed sheared by a viscous fluid. *Phys. Rev.* **93**, 012903 (2016).
31. C. Liu, A. De Luca, A. Rosso, L. Talon, Darcy's law for yield stress fluids. *Phys. Rev. Lett.* **122**, 245502 (2019).
32. N. Waisbord, N. Stoop, D. M. Walkama, J. Dunkel, J. S. Guasto, Anomalous percolation flow transition of yield stress fluids in porous media. *Phys. Rev. Fluids* **4**, 063303 (2019).
33. R. Dangla, S. Lee, C. N. Baroud, Trapping microfluidic drops in wells of surface energy. *Phys. Rev. Lett.* **107**, 124501 (2011).
34. H. Péter, A. Libál, C. Reichhardt, C. J. Reichhardt, Crossover from jamming to clogging behaviours in heterogeneous environments. *Sci. Rep.* **8**, 1–9 (2018).
35. M. C. Faleski, M. C. Marchetti, A. A. Middleton, Vortex dynamics and defects in simulated flux flow. *Phys. Rev. B* **54**, 12427–12436 (1996).
36. T. Sadhu, S. N. Majumdar, D. Mukamel, Long-range steady-state density profiles induced by localized drive. *Phys. Rev.* **84**, 051136 (2011).
37. R. Candelier, O. Dauchot, Creep motion of an intruder within a granular glass close to jamming. *Phys. Rev. Lett.* **103**, 128001 (2009).
38. V. Démery, O. Bénichou, H. Jacquin, Generalized Langevin equations for a driven tracer in dense soft colloids: Construction and applications. *New J. Phys.* **16**, 053032 (2014).
39. E. Nazockdast, J. F. Morris, Active microrheology of colloidal suspensions: Simulation and microstructural theory. *J. Rheol.* **60**, 733–753 (2016).
40. A. Poncet, O. Bénichou, V. Démery, G. Oshanin, Universal long ranged correlations in driven binary mixtures. *Phys. Rev. Lett.* **118**, 118002 (2017).
41. A. B. Kolton, D. Domínguez, N. Grønbech-Jensen, Hall noise and transverse freezing in driven vortex lattices. *Phys. Rev. Lett.* **83**, 3061–3064 (1999).
42. Y. Fily, E. Olive, N. Di Scala, J. C. Soret, Critical behavior of plastic depinning of vortex lattices in two dimensions: Molecular dynamics simulations. *Phys. Rev. B* **82**, 134519 (2010).
43. T. Vissers *et al.*, Lane formation in driven mixtures of oppositely charged colloids. *Soft Matter* **7**, 2352–2356 (2011).
44. M. Kohl, A. V. Ivlev, P. Brandt, G. E. Morfill, H. Löwen, Microscopic theory for anisotropic pair correlations in driven binary mixtures. *J. Phys. Condens. Matter* **24**, 464115 (2012).
45. N. Bain, D. Bartolo, Critical mingling and universal correlations in model binary active liquids. *Nat. Commun.* **8**, 1–6 (2017).
46. J. Watson, D. S. Fisher, Collective particle flow through random media. *Phys. Rev. B* **54**, 938 (1996).
47. A. Troyanovski, J. Aarts, P. Kes, Collective and plastic vortex motion in superconductors at high flux densities. *Nature* **399**, 665–668 (1999).
48. F. Pardo, F. De La Cruz, P. Gammel, E. Bucher, D. Bishop, Observation of smectic and moving-Bragg-glass phases in flowing vortex lattices. *Nature* **396**, 348–350 (1998).
49. L. Balents, M. C. Marchetti, L. Radzihovsky, Nonequilibrium steady states of driven periodic media. *Phys. Rev. B* **57**, 7705–7739 (1998).
50. N. Schorghofer, B. Jensen, A. Kudrolli, D. H. Rothman, Spontaneous channelization in permeable ground: Theory, experiment, and observation. *J. Fluid Mech.* **503**, 357–374 (2004).
51. A. Mahadevan, A. Orpe, A. Kudrolli, L. Mahadevan, Flow-induced channelization in a porous medium. *Europhys. Lett.* **98**, 58003 (2012).
52. A. Kudrolli, X. Clotet, Evolution of porosity and channelization of an erosive medium driven by fluid flow. *Phys. Rev. Lett.* **117**, 028001 (2016).
53. D. Bartolo, G. Degré, P. Nghe, V. Studer, Microfluidic stickers. *Lab Chip* **8**, 274–279 (2008).
54. B. Levaché, A. Azioune, M. Bourrel, V. Studer, D. Bartolo, Engineering the surface properties of microfluidic stickers. *Lab Chip* **12**, 3028–3031 (2012).
55. C. A. Schneider, W. S. Rasband, K. W. Eliceiri, NIH Image to ImageJ: 25 years of image analysis. *Nat. Methods* **9**, 671–675 (2012).
56. J. C. Crocker, D. G. Grier, Methods of digital video microscopy for colloidal studies. *J. Colloid Interface Sci.* **179**, 298–310 (1996).

Downloaded at Palestinian Territory, occupied on December 22, 2021

www.manaraa.com